JECS 2771p Disk used DTD = 4.1.0

Journal of the European Ceramic Society **19** (1999) 2211–2216
Published by Elsevier Science Ltd
Printed in Great Britain.
PII: S0955-2219(99)00126-0
0955-2219/99/$ - see front matter

A Combined Experimental and Theoretical Approach to Atomic Structure and Segregation at Ceramic Interfaces

S. J. Pennycook,[a]* E. C. Dickey,[b] P. D. Nellist,[c] M. F. Chisholm,[a] Y. Yan[a] and S. T. Pantelides[ad]

[a]Solid State Division, Oak Ridge National Laboratory, PO Box 2008, Oak Ridge, TN 37831-6030, USA
[b]Department of Chemical and Materials Engineering, University of Kentucky, 177 Anderson Hall, Lexington, KY 40506-0046, USA
[c]School of Physics and Astronomy, University of Birmingham, Birmingham B15 2TT, UK
[d]Department of Physics and Astronomy, Vanderbilt University, Nashville, TN 37235, USA

Abstract

In the last few years, the scanning transmission electron microscope has become capable of forming electron probes of atomic dimensions. This makes possible the technique of Z-contrast imaging, a method of forming direct images at atomic resolution with high compositional sensitivity. Atomic column positions can be determined to high accuracy from the image, and columns containing high-Z impurities will be visible. Atomic resolution electron energy loss spectroscopy is possible by locating the probe over particular atomic columns or planes seen in the image. This provides complementary information on low-Z species and chemical bonding. Such data represents an ideal starting point for first-principles theoretical calculations of energetics and dynamics, avoiding time-consuming searches of trial structures. Examples are shown of ordering in relaxor ferroelectrics, interfacial termination in oxide–oxide and metal–oxide interfaces, and an impurity-induced structural transformation of a ceramic grain boundary. Published by Elsevier Science Ltd.

Keywords: interfaces, simulation, electron microscopy, Z-contrast imaging, grain boundaries.

1 Introduction

In the scanning transmission electron microscope (STEM), the objective lens is designed to form a small electron probe which is scanned across a thin specimen as shown in the schematic of Fig. 1. With a crystalline specimen aligned along a low-index direction, the probe preferentially channels along the atomic columns, one by one as it is scanned across the specimen. A Z-contrast image results from mapping the total scattered intensity reaching an annular detector.[1–5] As high angle scattering comes predominantly from the atomic nuclei, bright features in the image correspond directly to columns of atoms, with the brightness approximately proportional to the mean square atomic number (Z). The image in Fig. 1 shows GaAs viewed along the [110] direction, and not only resolves the so-called 'dumbbell' spacing of 1·4 Å, but also distinguishes the Ga (Z = 31) column from the As (Z = 33) column. This mode of image formation differs significantly from that of conventional high resolution electron microscopy (HREM), in which contrast arises through the interference of a few diffracted beams. HREM is a coherent imaging technique, in which image contrast changes significantly with focus and sample thickness. This makes simulations essential for interpreting atom positions. Z-contrast imaging provides an incoherent image of the atomic structure, which has a direct and unique relationship to the object. It effectively bypasses the phase problem of HREM, and allows the positions of atomic columns to be determined directly from the image to a high accuracy. By avoiding the reliance on simulations of model structures, the Z-contrast image is sensitive to unexpected atomic arrangements, such as interfacial phases or transition zones. For theoretical studies, it avoids the need to search through large numbers of trial atomic configurations, with enormous savings in computer time, a particular advantage for multicomponent materials.

As apparent from Fig. 1, electron energy loss spectroscopy (EELS) can be performed simultaneously with the Z-contrast image. In fact, the Z-contrast

*To whom correspondence should be addressed.

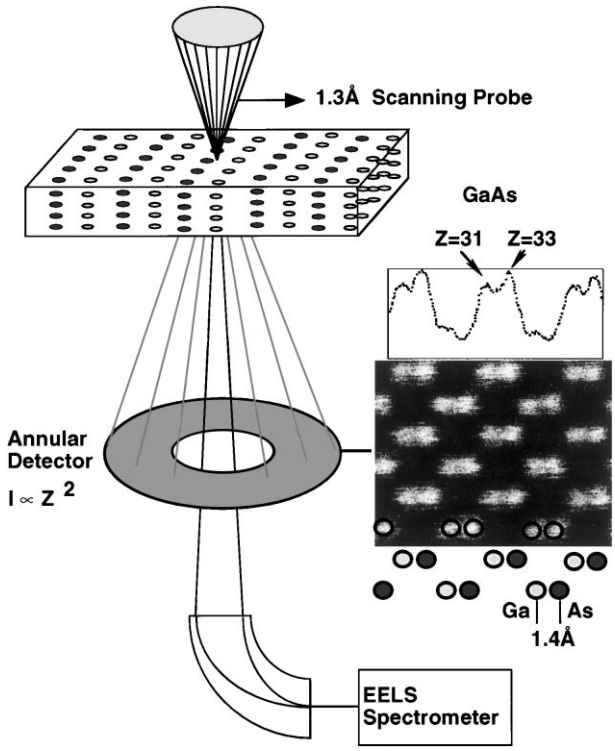

Fig. 1. Schematic showing Z-contrast imaging and atomic resolution electron energy loss spectroscopy on a STEM. The image of GaAs resolves the dumbbells and distinguishes the sublattice polarity as seen from the intensity profile.

image allows the electron probe to be located over particular atomic columns seen in the image, allowing atomic resolution chemical analysis to be achieved.[6,7] EELS is sensitive to elements such as oxygen and nitrogen which are too light to contribute to the Z-contrast image. In addition, the fine structure on the core loss absorption edge maps the density of empty states at the particular species in the atomic column illuminated by the probe. Since the probe can illuminate a single column of atoms at an interface, local changes in band structure, impurity concentration, valence and bond angles can be detected. This is particularly valuable at a crystal/amorphous interface where it gives direct information on the structure and composition in the amorphous phase adjacent to the last crystalline plane.

The microscope used for the images presented here is a VG Microscopes HB603U, with a 300 kV accelerating voltage and a resolution (probe size) of 1·26 Å. EELS is performed with a 100 kV STEM, a VG Microscopes HB501UX, which has a probe size of 2·2 Å. In this paper we present examples of the imaging of ordered domains in relaxor ferroelectrics, showing that the ordering follows the charge-balanced random layer model. We then present the determination of interfacial structure and bonding in the NiO/ZrO_2 and Ni/ZrO_2 systems, demonstrating the sensitivity with which metallic and ionic bonding can be distinguished. Finally, we show the direct imaging of Ca impurity sites in a MgO grain boundary. The structure is seen to be different to that predicted and observed in previous studies. First-principles calculations resolve the apparent discrepancy, by showing that the segregation of Ca has induced a structural transformation to a more dense grain boundary structure.

2. Ordering in Ferroelectric Perovskites

The nature of the ordered structure of the lead-based relaxor ferroelectric $Pb(Mg_{1/3}Nb_{2/3})O_3$ (PMN) has been the subject of controversy. Two models have been proposed for the ordering, the space-charge model and the charge-balanced random-layer model.[8,9] These models differ in the distribution of the B-site cations in the doubled unit cell. In the space-charge model, the B^{I} and B^{II} sites are occupied exclusively by the Mg^{2+} and Nb^{5+} cations, respectively, in the form $Pb(Mg_{1/2}Nb_{1/2})O_3$. The resulting net negative charge is assumed compensated by a disordered, Nb^{5+} rich matrix. In the charge-balanced random-layer model, microscopic charge balance is achieved by occupying the B^{II} columns exclusively by Nb^{5+} and the B^{I} columns with a random distribution of Mg^{2+} and Nb^{5+} in a 2:1 ratio. Z-contrast imaging along the [110] zone axis can easily distinguish these two cases. In the space charge structure, the ratio of B^{I} column (Mg) to B^{II} column (Nb) intensities is given by approximately 1/17, whereas, in the charge-balanced random-layer structure it is close to 1/4.

Figure 2(a) shows a Z-contrast image of 25% La-doped PMN.[10] The La doping increases the grain size significantly, ensuring that a single domain exists throughout the thickness of the region imaged. The intensity trace taken through the B sublattice clearly shows the intensity ratio is consistent with the 1/4 value expected for the charge-balanced random-layer model. For comparison, Fig. 2(b) shows an image and line trace from $Ba(Mg_{1/3}Nb_{2/3})O_3$ in which the B sites are fully occupied by either Mg or Nb in a 2:1 ratio. The line trace shows the expected very weak intensity from the Mg column. A somewhat higher intensity is observed from the Mg site on the left hand side, indicating that the ordering is not entirely complete. Images were also taken from thin, undoped PMN. Although the contrast was often reduced due to the overlap of small domains through the sample thickness, the maximum value seen was still 1/4. This indicates that the ordered structure of undoped PMN also follows the charge-balanced random-layer model.

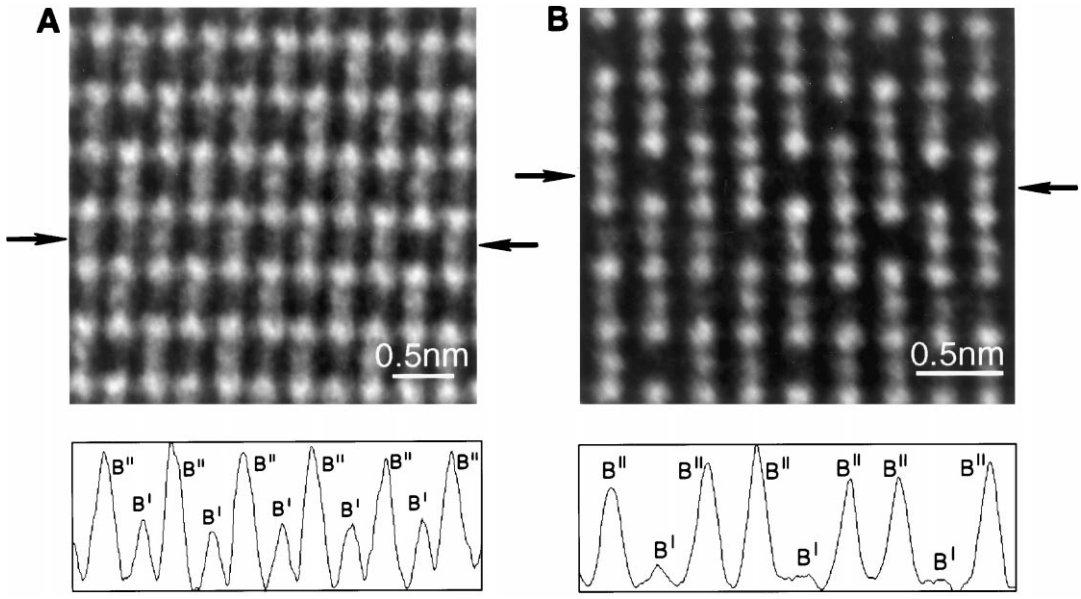

Fig. 2. Z-contrast images of (a) 25% La-doped $Pb(Mg_{1/3}Nb_{2/3})O_3$, (b) $Ba(Mg_{1/3}Nb_{2/3})O_3$ with intensity profiles across the B sublattice showing the PMN to have the charge-balanced random layer structure.

3. Determination of Interfacial Structure and Bonding

The nature of interfacial bonding critically determines the mechanical properties of ceramic/ceramic and metal/ceramic interfaces, and has therefore been the focus of many HREM investigations. Here we demonstrate the sensitivity with which the nature of interfacial bonding can be established by the combination of Z-contrast imaging and EELS, using a model system, a NiO/ZrO_2(cubic) directionally-solidified eutectic.[10,11] This system is known to undergo electrochemical reduction to form Ni/ZrO_2(cubic) interfaces, the oxygen removal being mediated by fast ionic conduction through the ZrO_2. In our case, reduction was performed *in situ*, through electron beam irradiation, allowing us to study the oxidized and reduced interfaces in the same sample.

Figure 3 shows a Z-contrast image of the oxidized interface, with NiO[$\bar{1}$10]// ZrO_2[010]. Of the several possible interface structures, one fits precisely over the experimental image, as shown in the figure. Clearly this interface is atomically abrupt. It is also apparent that the interface is coherent, consistent with the 0·4% mismatch in lattice parameters between NiO(111) and ZrO_2 (200) planar spacings across the interface. A Z-contrast image from a sample in the orthogonal direction, NiO[11$\bar{2}$] // ZrO_2[001], is shown in Fig. 4, in which the 1·48 Å NiO(220) spacing is resolved. Visible in the last NiO plane before the interface is the presence of local atomic relaxations as indicated schematically on the figure. Pairs of NiO(220) planes relax towards each other, to match the 2·57 Å (200) spacing in the ZrO_2. The (110) spacing of NiO is

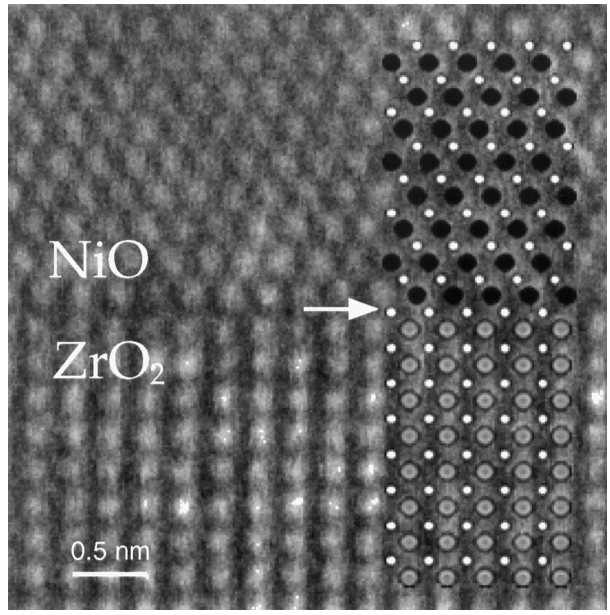

Fig. 3. Z-contrast image of a NiO-ZrO_2 interface viewed along the NiO[-110] direction. Superposed structure model shows the presence of a common oxygen plane (arrowed). Oxygen atoms are shown as small white circles, Ni as black circles and Zr as grey circles.

15% larger, and indeed we see misfit dislocations at this interface comprising missing NiO(220) planes with approximately the expected frequency, as indicated in Fig. 4. Combining the information from the two projections gives the three-dimensional atomic structure of this interface.

Atomic positions were quantified by maximum entropy reconstruction, with an accuracy of ±0·1 Å.[13] In this way the spacing between the terminating Ni and Zr planes was determined to be 2·71 Å, intermediate between the 2·57 Å (200) spacing in the ZrO_2 and the 2·51 Å (111) spacing in the NiO, precisely as

would be expected on the basis of a common oxygen plane. Confirmation of the presence of an interfacial oxygen plane is provided by EELS profiles recorded plane-by-plane across the interface, shown in Fig. 5. The widths of the Ni and Zr profiles are consistent with a chemically abrupt interface, and the oxygen concentration at the interface is seen to be intermediate between that in NiO and ZrO_2, again indicative of a common oxygen plane.

Figure 6 shows a Z-contrast image together with a maximum entropy reconstruction of the reduced Ni–ZrO_2 interface. Again, misfit dislocations are visible at the interface. Now, however, the spacing between the terminating Ni and Zr planes is determined to be 2·24 Å, a significant reduction compared to the oxide/oxide interface, suggesting that oxygen has been removed from the interface. Confirmation of this is provided by EELS. Figure 7 shows the EELS spectra from the interface compared to spectra recorded from nearby Ni and NiO. It is immediately clear that the interface spectrum is similar to that of the Ni metal; the strong white lines, characteristic of the oxide, are absent. Also shown is a difference spectrum that again shows no evidence of NiO from the interface. Quantitative comparison of the spectra indicates that less than 4% contribution of the NiO edge fine structure to the interface spectrum. Although isolated O atoms at the interface may not show the fine structure characteristic of fully oxidized NiO, this is a strong indication that the bonding is now predominantly metallic in nature.

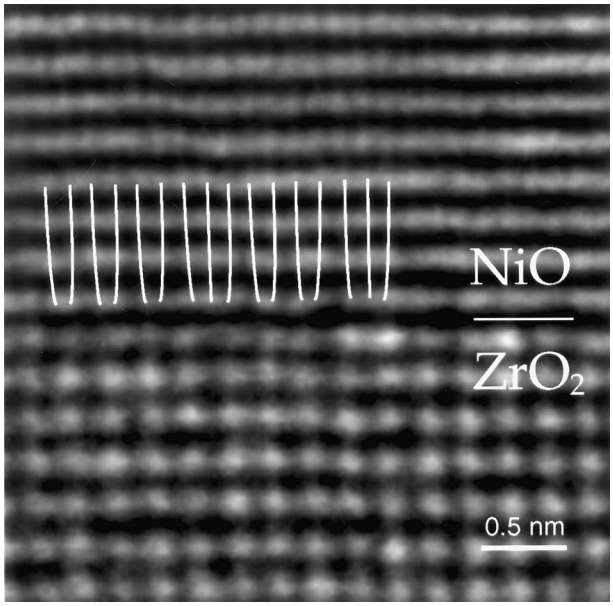

Fig. 4. Z-contrast image of the NiO-ZrO_2 interface viewed along the perpendicular NiO[11$\bar{2}$] direction. Local atomic relaxations and misfit dislocations are indicated.

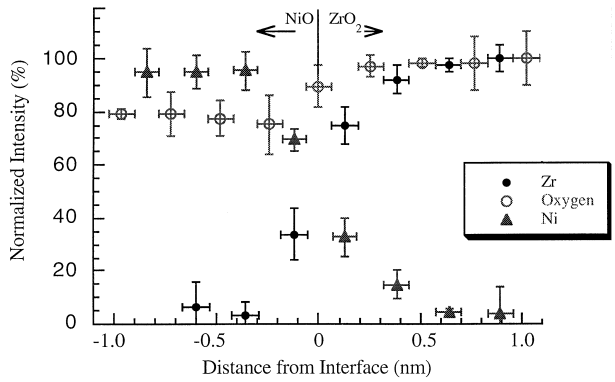

Fig. 5. EELS profiles recorded plane by plane across the NiO-ZrO_2 interface confirming the presence of a common oxygen plane at the interface.

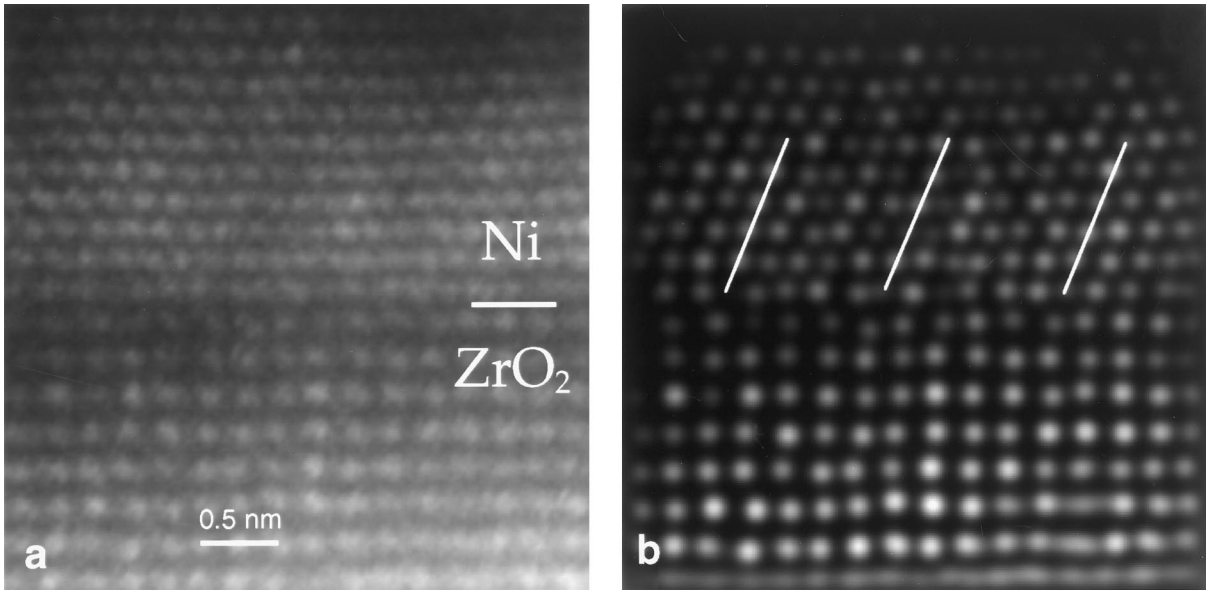

Fig. 6. Z-contrast image and maximum entropy reconstruction of a Ni-ZrO_2 interface produced *in situ* from the NiO–ZrO_2 interface by electron beam induced reduction. Misfit dislocations are indicated.

4. Impurity-Induced Grain Boundary Transformation in MgO

In this example, STEM imaging of an MgO grain boundary (Fig. 8)[14] revealed a structure that was inconsistent with the widely accepted structure of that boundary proposed by Harris *et al.*[15] based on theoretical modelling using classical potentials. The observed structure was similar to that proposed much earlier by Kingery.[16] These two structures are compared in Fig. 9, where the large empty core of the Harris structure is obviously very different from the more dense core of the Kingery model. On careful examination of the intensity in the experimental image, it can be seen that certain specific atomic columns at the grain boundary are significantly brighter than neighboring columns, as arrowed in the figure. This suggests that impurities, with $Z > 12$, may be segregated at these sites. EELS measurements (Fig. 10) indeed established that significant concentrations of Ca are present in

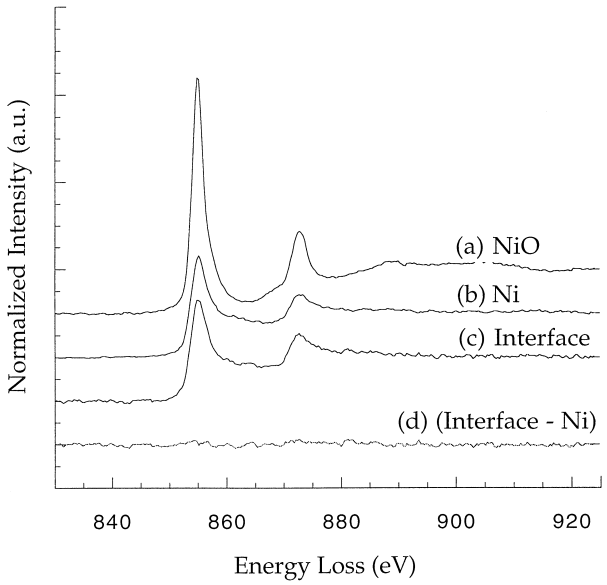

Fig. 7. Ni L-edge EELS spectra recorded from the Ni–ZrO_2 interface compared to spectra from the nearby Ni metal and NiO. The difference between the Ni metal and the interface spectra is almost featureless, indicating metallic bonding between the terminating Ni and Zr planes.

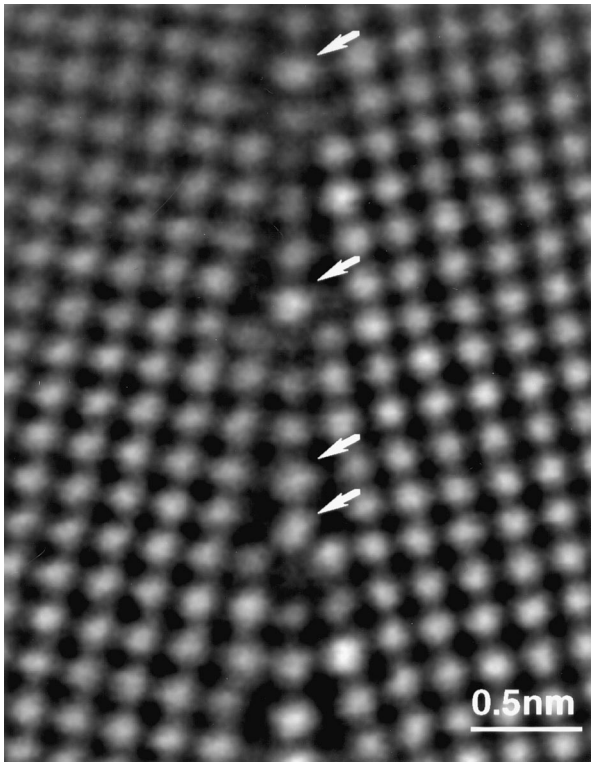

Fig. 8. Z-contrast image from a 24° < 001 > tilt grain boundary in MgO showing occasional bright atomic columns at the grain boundary (arrowed).

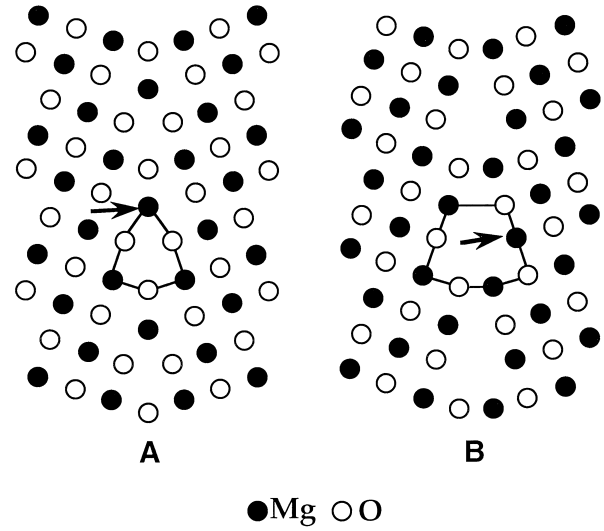

Fig. 9. Comparison of the structures for the 36° < 001 > tilt grain boundary in MgO proposed by (a) Harris *et al.*[15] and (b) Kingery.[16] The atomic arrangements seen in the experimental image are similar to those in the Harris structure. Sites of Ca segregation are arrowed.

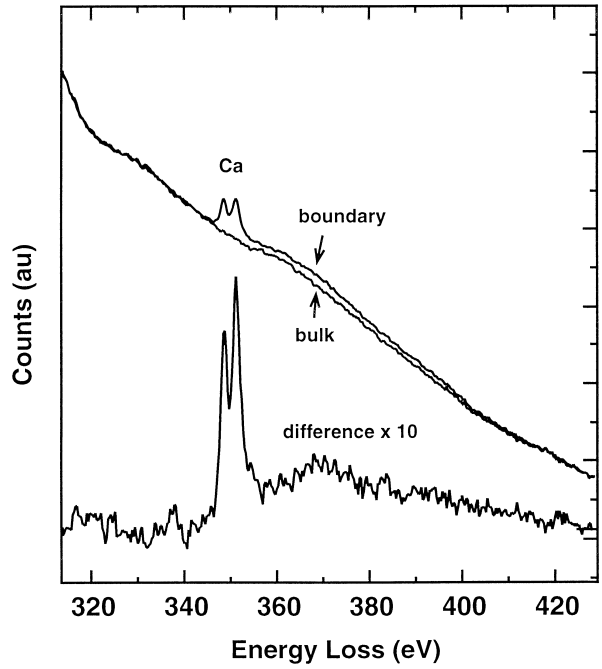

Fig. 10. EELS spectra from the MgO grain boundary and nearby bulk, and their difference, showing Ca segregation.

the grain boundary, 0·3 monolayers, consistent with the bright intensity in the image.

To reconcile these observations with the prior experimental and theoretical work, first-principles theoretical calculations were performed. These calculations in fact reproduced the results of the classical potential calculations for the clean grain boundary, indicating the open structure to be 0·5 eV lower in energy per periodic repeat unit. Theory further determined that Ca has a large segregation energy in both boundary structures, but *significantly higher* in the dense structure, sufficient to make the dense structure the lower energy boundary. These calculations therefore establish that the dense structure is in fact *stabilized* by the Ca segregation, a segregation induced structural transformation. Examination of the electronic charge distribution revealed just a small perturbation to the oxygen ions next to the Ca atom, indicating the transformation is structural not electronic in origin, i.e. it is driven by the size difference between Ca and Mg. These insights would be impossible without a synergistic combination of theory and experiment.

5. Conclusions

It is now possible to determine, without prior knowledge, the structure, impurity content and local electronic states at ceramic interfaces, including amorphous/crystal interfaces, by a combination of experimental and theoretical methods. Although the particular microscopes used here are no longer commercially available, conventional TEM instruments are now capable of forming probes of less than 2 Å in diameter. Atomic-scale total energy calculations are a natural complement and extension to these STEM techniques, giving critical insight into the underlying reasons for materials properties through the ability to study segregation energies, electronic states, and atomic scale dynamics. With this combined approach, using state-of-the-art microscopes and supercomputers, it is feasible to understand interfacial bond strength and interfacial diffusion mechanisms at the atomic level, and so finally to understand the fundamental factors controlling strength and creep phenomena in high temperature ceramics.

Acknowledgements

The authors would like to thank D. J. Wallis, G. Duscher, Z. Xu, D., Viehland, N. D. Browning and V. P. Dravid for research collaborations. This research was supported by Lockheed Martin Energy Research Corp. under DOE Contract No. DE-AC05-96OR22464, by ONR Grant No. N00014-95-1-0906, and by an appointment to the ORNL Postdoctoral Research Associates Program administered jointly by ORNL and ORISE.

References

1. Pennycook, S. J. and Jesson, D. E., *Phys. Rev. Lett*., 1990, **64**, 938.
2. Pennycook, S. J. and Jesson, D. E., *Acta. Metall. Mater*., 1992, **40**, S149.
3. Pennycook, S. J., *Annu. Rev. Mater. Sci*., 1992, **22**, 171.
4. Pennycook, S. J., *Phil. Trans. Roy. Soc. A*, 1996, **354**, 2619.
5. Pennycook, S. J. *et al*., In *Handbook of Microscopy*, ed. S. Amelinckx, G. Van Tendeloo, D. Van Dyck and J. Van Landuyt. VCH Publishers, Weinheim, Germany, 1997, p.595.
6. Browning, N. D., Chisholm, M. F. and Pennycook, S. J., *Nature*, 1993, **366**, 143.
7. Duscher, G., Browning, N. D. and Pennycook, S. J., *Phys. Stat. Sol. A*, 1998, **166**, 327.
8. Chen, J., Chan, H. M. and Harmer, M. P., *J. Am. Ceram. Soc*., 1989, **72**, 593.
9. Randall, C. and Bhalla, A., *Jpn. J. Appl. Phys., Part 1*, 1990, **29**, 327.
10. Yan, Y., Pennycook, S. J., Xu, Z. and Viehland, D., *Appl. Phys. Letts*, 1998, **72**, 3145.
11. Dickey, E. C., *Microsc. and Microan*., 1997, **3**, 443.
12. Dickey, E. C., *Acta Mater*., 1998, **46**, 1801.
13. Nellist, P. D. and Pennycook, S. J., *J. Microsc*., 1998, **190**, 159.
14. Yan, Y., Chisholm, M. F., Duscher, G. and Pennycook, S. J., *J. Elect. Microsc*., 1998, **47**, 115.
15. Harris, D. M., Watson, G. W. and Parker, S. C., *Phil. Mag*., 1996, **A74**, 407.
16. Kingery, W. D., *J. Am. Cer. Soc*., 1974, **57**, 1.